The Astrophysical Journal Letters, 978:L29 (14pp), 2025 January 10 https://doi.org/10.3847/2041-8213/ad99d3

The NANOGrav 15 yr Data Set: Running of the Spectral Index

Gabriella Agazie[1], Akash Anumarlapudi[1], Anne M. Archibald[2], Zaven Arzoumanian[3], Jeremy G. Baier[4], Paul T. Baker[5], Bence Bécsy[4], Laura Blecha[6], Adam Brazier[7,8], Paul R. Brook[9], Sarah Burke-Spolaor[10,11,68], J. Andrew Casey-Clyde[12], Maria Charisi[13], Shami Chatterjee[7], Tyler Cohen[14], James M. Cordes[7], Neil J. Cornish[15], Fronefield Crawford[16], H. Thankful Cromartie[17,72], Kathryn Crowter[18], Megan E. DeCesar[19,72], Paul B. Demorest[20], Heling Deng[4], Lankeswar Dey[10,11], Timothy Dolch[21,22], David Esmyol[23], Elizabeth C. Ferrara[24,25,26], William Fiore[10,11], Emmanuel Fonseca[10,11], Gabriel E. Freedman[1], Emiko C. Gardiner[27], Nate Garver-Daniels[10,11], Peter A. Gentile[10,11], Kyle A. Gersbach[13], Joseph Glaser[10,11], Deborah C. Good[28], Kayhan Gültekin[29], Jeffrey S. Hazboun[4], Ross J. Jennings[10,11,69], Aaron D. Johnson[1,30], Megan L. Jones[1], David L. Kaplan[1], Luke Zoltan Kelley[27], Matthew Kerr[31], Joey S. Key[32], Nima Laal[4], Michael T. Lam[33,34,35], William G. Lamb[13], Bjorn Larsen[36], T. Joseph W. Lazio[37], Natalia Lewandowska[38], Rafael R. Lino dos Santos[39], Tingting Liu[10,11], Duncan R. Lorimer[10,11], Jing Luo[40,70], Ryan S. Lynch[41], Chung-Pei Ma[27,42], Dustin R. Madison[43], Alexander McEwen[1], James W. McKee[44,45], Maura A. McLaughlin[10,11], Natasha McMann[13], Bradley W. Meyers[18,46], Patrick M. Meyers[30], Chiara M. F. Mingarelli[36], Andrea Mitridate[47], Cherry Ng[48], David J. Nice[49], Stella Koch Ocker[30,50], Ken D. Olum[51], Timothy T. Pennucci[52], Benetge B. P. Perera[53], Nihan S. Pol[54], Henri A. Radovan[55], Scott M. Ransom[56], Paul S. Ray[31], Joseph D. Romano[54], Jessie C. Runnoe[13], Alexander Saffer[56,69], Shashwat C. Sardesai[1], Ann Schmiedekamp[57], Carl Schmiedekamp[57], Kai Schmitz[23], Tobias Schröder[23], Brent J. Shapiro-Albert[10,11,58], Xavier Siemens[1,4], Joseph Simon[59,71], Magdalena S. Siwek[60], Sophia V. Sosa Fiscella[34,35], Ingrid H. Stairs[18], Daniel R. Stinebring[61], Kevin Stovall[20], Abhimanyu Susobhanan[62], Joseph K. Swiggum[49,69], Stephen R. Taylor[13], Jacob E. Turner[41], Caner Unal[63,64,65], Michele Vallisneri[30,37], Rutger van Haasteren[62], Sarah J. Vigeland[1], Richard von Eckardstein[23], Haley M. Wahl[10,11], Caitlin A. Witt[66,67], David Wright[4], and Olivia Young[34,35]

[1] Center for Gravitation, Cosmology and Astrophysics, Department of Physics, University of Wisconsin–Milwaukee, P.O. Box 413, Milwaukee, WI 53201, USA
[2] Newcastle University, NE1 7RU, UK
[3] X-Ray Astrophysics Laboratory, NASA Goddard Space Flight Center, Code 662, Greenbelt, MD 20771, USA
[4] Department of Physics, Oregon State University, Corvallis, OR 97331, USA
[5] Department of Physics and Astronomy, Widener University, One University Place, Chester, PA 19013, USA
[6] Physics Department, University of Florida, Gainesville, FL 32611, USA
[7] Cornell Center for Astrophysics and Planetary Science and Department of Astronomy, Cornell University, Ithaca, NY 14853, USA
[8] Cornell Center for Advanced Computing, Cornell University, Ithaca, NY 14853, USA
[9] Institute for Gravitational Wave Astronomy and School of Physics and Astronomy, University of Birmingham, Edgbaston, Birmingham B15 2TT, UK
[10] Department of Physics and Astronomy, West Virginia University, P.O. Box 6315, Morgantown, WV 26506, USA
[11] Center for Gravitational Waves and Cosmology, West Virginia University, Chestnut Ridge Research Building, Morgantown, WV 26505, USA
[12] Department of Physics, University of Connecticut, 196 Auditorium Road, U-3046, Storrs, CT 06269-3046, USA
[13] Department of Physics and Astronomy, Vanderbilt University, 2301 Vanderbilt Place, Nashville, TN 37235, USA
[14] Department of Physics, New Mexico Institute of Mining and Technology, 801 Leroy Place, Socorro, NM 87801, USA
[15] Department of Physics, Montana State University, Bozeman, MT 59717, USA
[16] Department of Physics and Astronomy, Franklin & Marshall College, P.O. Box 3003, Lancaster, PA 17604, USA
[17] National Research Council Research Associate, National Academy of Sciences, Washington, DC 20001, USA
[18] Department of Physics and Astronomy, University of British Columbia, 6224 Agricultural Road, Vancouver, BC V6T 1Z1, Canada
[19] George Mason University, Fairfax, VA 22030, USA
[20] National Radio Astronomy Observatory, 1003 Lopezville Road, Socorro, NM 87801, USA
[21] Department of Physics, Hillsdale College, 33 East College Street, Hillsdale, MI 49242, USA
[22] Eureka Scientific, 2452 Delmer Street, Suite 100, Oakland, CA 94602-3017, USA
[23] Institute for Theoretical Physics, University of Münster, 48149 Münster, Germany; kai.schmitz@nanograv.org
[24] Department of Astronomy, University of Maryland, College Park, MD 20742, USA
[25] Center for Research and Exploration in Space Science and Technology, NASA/GSFC, Greenbelt, MD 20771, USA
[26] NASA Goddard Space Flight Center, Greenbelt, MD 20771, USA
[27] Department of Astronomy, University of California, Berkeley, 501 Campbell Hall #3411, Berkeley, CA 94720, USA
[28] Department of Physics and Astronomy, University of Montana, 32 Campus Drive, Missoula, MT 59812, USA
[29] Department of Astronomy and Astrophysics, University of Michigan, Ann Arbor, MI 48109, USA
[30] Division of Physics, Mathematics, and Astronomy, California Institute of Technology, Pasadena, CA 91125, USA
[31] Space Science Division, Naval Research Laboratory, Washington, DC 20375-5352, USA
[32] University of Washington Bothell, 18115 Campus Way NE, Bothell, WA 98011, USA
[33] SETI Institute, 339 North Bernardo Avenue Suite 200, Mountain View, CA 94043, USA
[34] School of Physics and Astronomy, Rochester Institute of Technology, Rochester, NY 14623, USA
[35] Laboratory for Multiwavelength Astrophysics, Rochester Institute of Technology, Rochester, NY 14623, USA
[36] Department of Physics, Yale University, New Haven, CT 06520, USA
[37] Jet Propulsion Laboratory, California Institute of Technology, 4800 Oak Grove Drive, Pasadena, CA 91109, USA
[38] Department of Physics and Astronomy, State University of New York at Oswego, Oswego, NY 13126, USA
[39] National Centre for Nuclear Research, Pasteura 7, 02-093 Warsaw, Poland; rafaellinodossantos@nanograv.org
[40] Department of Astronomy & Astrophysics, University of Toronto, 50 St. George Street, Toronto, ON M5S 3H4, Canada
[41] Green Bank Observatory, P.O. Box 2, Green Bank, WV 24944, USA
[42] Department of Physics, University of California, Berkeley, CA 94720, USA
[43] Department of Physics, University of the Pacific, 3601 Pacific Avenue, Stockton, CA 95211, USA

[44] E.A. Milne Centre for Astrophysics, University of Hull, Cottingham Road, Kingston-upon-Hull, HU6 7RX, UK
[45] Centre of Excellence for Data Science, Artificial Intelligence and Modelling (DAIM), University of Hull, Cottingham Road, Kingston-upon-Hull, HU6 7RX, UK
[46] International Centre for Radio Astronomy Research, Curtin University, Bentley, WA 6102, Australia
[47] Deutsches Elektronen-Synchrotron DESY, Notkestr. 85, 22607 Hamburg, Germany
[48] Dunlap Institute for Astronomy and Astrophysics, University of Toronto, 50 St. George Street, Toronto, ON M5S 3H4, Canada
[49] Department of Physics, Lafayette College, Easton, PA 18042, USA
[50] The Observatories of the Carnegie Institution for Science, Pasadena, CA 91101, USA
[51] Institute of Cosmology, Department of Physics and Astronomy, Tufts University, Medford, MA 02155, USA
[52] Institute of Physics and Astronomy, Eötvös Loránd University, Pázmány P. s. 1/A, 1117 Budapest, Hungary
[53] Arecibo Observatory, HC3 Box 53995, Arecibo, PR 00612, USA
[54] Department of Physics, Texas Tech University, Box 41051, Lubbock, TX 79409, USA
[55] Department of Physics, University of Puerto Rico, Mayagüez, PR 00681, USA
[56] National Radio Astronomy Observatory, 520 Edgemont Road, Charlottesville, VA 22903, USA
[57] Department of Physics, Penn State Abington, Abington, PA 19001, USA
[58] Giant Army, 915A 17th Avenue, Seattle, WA 98122, USA
[59] Department of Astrophysical and Planetary Sciences, University of Colorado, Boulder, CO 80309, USA
[60] Center for Astrophysics, Harvard University, 60 Garden Street, Cambridge, MA 02138, USA
[61] Department of Physics and Astronomy, Oberlin College, Oberlin, OH 44074, USA
[62] Max-Planck-Institut für Gravitationsphysik (Albert-Einstein-Institut), Callinstrasse 38, D-30167, Hannover, Germany
[63] Department of Physics, Middle East Technical University, 06531 Ankara, Turkey
[64] Department of Physics, Ben-Gurion University of the Negev, Be'er Sheva 84105, Israel
[65] Feza Gursey Institute, Bogazici University, Kandilli, 34684, Istanbul, Turkey
[66] Center for Interdisciplinary Exploration and Research in Astrophysics (CIERA), Northwestern University, Evanston, IL 60208, USA
[67] Adler Planetarium, 1300 South DuSable Lake Shore Drive, Chicago, IL 60605, USA
Received 2024 October 12; revised 2024 November 21; accepted 2024 November 28; published 2025 January 6

Abstract

The NANOGrav 15 yr data provide compelling evidence for a stochastic gravitational-wave (GW) background at nanohertz frequencies. The simplest model-independent approach to characterizing the frequency spectrum of this signal consists of a simple power-law fit involving two parameters: an amplitude A and a spectral index γ. In this Letter, we consider the next logical step beyond this minimal spectral model, allowing for a *running* (i.e., logarithmic frequency dependence) of the spectral index, $\gamma_{\rm run}(f) = \gamma + \beta \ln(f/f_{\rm ref})$. We fit this running-power-law (RPL) model to the NANOGrav 15 yr data and perform a Bayesian model comparison with the minimal constant-power-law (CPL) model, which results in a 95% credible interval for the parameter β consistent with no running, $\beta \in [-0.80, 2.96]$, and an inconclusive Bayes factor, $\mathcal{B}(\text{RPL} \quad \text{versus} \quad \text{CPL}) = 0.69 \pm 0.01$. We thus conclude that, at present, the minimal CPL model still suffices to adequately describe the NANOGrav signal; however, future data sets may well lead to a measurement of nonzero β. Finally, we interpret the RPL model as a description of primordial GWs generated during cosmic inflation, which allows us to combine our results with upper limits from Big Bang nucleosynthesis, the cosmic microwave background, and LIGO–Virgo–KAGRA.

Unified Astronomy Thesaurus concepts: Pulsar timing method (1305); Gravitational waves (678); Bayesian statistics (1900); Cosmic inflation (319); Cosmology (343); Cosmic microwave background radiation (322); High energy astrophysics (739)

1. Introduction

Pulsar timing arrays (PTAs) are gravitational-wave (GW) detectors of galactic dimensions that aim to measure the imprint of a nanohertz GW background (GWB) in the timing data of millisecond pulsars (S. R. Taylor 2021). Recently, the field of PTA searches for GWs reached an important milestone when the CPTA (H. Xu et al. 2023), EPTA and InPTA (J. Antoniadis et al. 2023), NANOGrav (G. Agazie et al. 2023a), and PPTA (D. J. Reardon et al. 2023) Collaborations announced the first observational evidence for the Hellings–Downs (HD) curve (R. W. Hellings & G. S. Downs 1983), i.e., the characteristic cross-correlation pattern that general relativity predicts a GWB to induce in the timing-residual cross-power spectrum for pairs of pulsars in the sky. The NANOGrav 15 yr (NG15) data (G. Agazie et al. 2023b) in particular provide compelling evidence for the presence of an HD-correlated common-spectrum process (i.e., a GWB) at nanohertz frequencies at a level of statistical significance of $3.5\sigma \cdots 4.0\sigma$ (G. Agazie et al. 2023a).

Assuming the signal in the NG15 data to correspond to a genuine GWB, one is faced with the question of its origin. The most common expectation is that the signal is caused by a cosmic population of inspiraling supermassive black-hole binaries (SMBHBs) at the centers of galaxies (G. Agazie et al. 2023c). Alternatively, it may represent a GW echo of the Big Bang, i.e., a primordial GWB signal produced by new particle physics in the very early Universe (C. Caprini & D. G. Figueroa 2018; A. Afzal et al. 2023; J. Antoniadis et al. 2024). In order to resolve this dichotomy and pin down the origin of the signal, more work is needed. In the coming years, searches for continuous-wave signals (G. Agazie et al. 2023d) and GWB anisotropies (G. Agazie et al. 2023e) promise to shed more light on the origin of the signal. However, for the time

[68] Sloan Fellow.
[69] NANOGrav Physics Frontiers Center Postdoctoral Fellow.
[70] Deceased.
[71] NSF Astronomy and Astrophysics Postdoctoral Fellow.
[72] Resident at the U.S. Naval Research Laboratory, Washington, DC 20375, USA.

being, model selection mostly relies on the spectral characterization of the signal (W. G. Lamb et al. 2023; A. Mitridate et al. 2023; K. A. Gersbach et al. 2024), which is what we will be concerned with in this Letter.

Explicit astrophysical and cosmological models often yield specific predictions for the spectral shape of the GWB. For instance, the simplest SMBHB models, in which binary evolution is purely driven by GW emission, predict a power-law shape with a characteristic spectral index, $\gamma \simeq 13/3$ (see below for the definition of γ), in the limit of a large number of sources (E. S. Phinney 2001). The GW signal from a first-order phase transition in the early Universe, on the other hand, is expected to have the shape of a broken power law or even a doubly broken power law (C. Caprini et al. 2024). These predictions are representative of the top-down approach to the spectral characterization of the signal, i.e., the idea to first start from a concrete physical model (possibly involving physics at very high energies) and then work out the observational consequences in the PTA frequency band. In parallel, it is imperative to develop model-independent spectral templates that enable a bottom-up approach to the spectral characterization of the signal, i.e., an approach that starts with an agnostic description of features in the data and then asks which GWB models might be able to account for these features. At present, two model-independent templates are commonly used in the PTA literature: (i) a simple power law, parameterized in terms of an amplitude A (at some reference frequency $f_{\rm ref}$) and a spectral index γ, and (ii) a free spectrum, which treats the GWB amplitude in each frequency bin as a free parameter. The purpose of the present Letter is to extend this list of templates by a third one.

The power-law template clearly represents the simplest model-independent ansatz for the spectral shape of the GWB. The spectral index γ in this model is assumed to be constant, which is why we will refer to this model as the constant-power-law (CPL) model in the following. If plotted on doubly logarithmic axes, the function graph of a power law is nothing but a straight line. Therefore, if we seek to construct next-to-minimal GWB templates, the next logical step beyond a CPL is what we will refer to as a running power law (RPL), a model in which the spectral index is allowed to exhibit a logarithmic frequency dependence,

$$\gamma_{\rm run}(f) = \gamma + \beta \ln\left(\frac{f}{f_{\rm ref}}\right). \tag{1}$$

As we will see shortly, the RPL model describes parabola-shaped GWB spectra, if plotted on doubly logarithmic axes, rendering it a natural generalization of the CPL model. While the RPL model has received only a little attention in the PTA literature thus far (see I. Ben-Dayan et al. 2023 for a notable exception), similar constructions are well established in the literature on the cosmic microwave background (CMB). In their analysis of the primordial curvature power spectrum, the PLANCK Collaboration, e.g., uses their CMB data to constrain the "running of the scalar spectral index" and even the "running of the running of the scalar spectral index" (N. Aghanim 2020; Y. Akrami et al. 2020). The goal of the present Letter is to introduce some of these ideas to the PTA community and initiate a systematic investigation of observational limits on the running of the spectral index in the PTA band, i.e., the parameter

$$\beta = \frac{d\gamma_{\rm run}(f)}{d\ln f}. \tag{2}$$

The RPL model promises to serve as a better proxy for many GWB candidate models that have been proposed as a possible explanation for the signal in the PTA frequency band than the CPL model. On the astrophysical side, this is true because SMBHB models often predict a spectral turnover at low frequencies due to interactions with the circumbinary environment (B. Kocsis & A. Sesana 2011; G. Agazie et al. 2023c), alongside a spectral break at high frequencies caused by the discrete nature of the SMBHB population (A. Sesana et al. 2008; G. Agazie et al. 2025). While other templates may be able to describe such features even better, the RPL model can at least roughly account for the presence of a spectral turnover or break, while the CPL model has no chance of doing so whatsoever. The real strength of the RPL model, however, lies in the fact that it can serve as a good or even very good approximation of many cosmological models. The spectral index of cosmological signals often varies slowly across several orders of magnitude in frequency space, which results in a mild running of the spectral index in the PTA frequency band and hence gives rise to an RPL-like spectral shape. We therefore argue that bounds on the three parameters of the RPL model—the amplitude A at $f = f_{\rm ref}$, the spectral index γ at $f = f_{\rm ref}$, and the running of the spectral index β—provide valuable information that can be used to constrain a large class of cosmological models. In this Letter, we will fit the RPL model to the NG15 data to derive Bayesian limits on A, γ, and β of exactly this type.

The rest of this Letter is organized as follows. In the next section, we will properly define the RPL model and discuss some of its properties. In Section 3, we will then perform a Bayesian fit of the RPL model to the NG15 data. This analysis will provide us with marginalized posterior distributions for the parameters A, γ, and β, which we will use to construct Bayesian 95% credible intervals for all three parameters. Furthermore, we will carry out a Bayesian model comparison with the CPL model and determine the RPL-versus-CPL Bayes factor. In Section 4, we will subsequently broaden the scope of our analysis and interpret the RPL model as a description of primordial GWs from cosmic inflation. This means we will extrapolate our results to frequencies above and below the PTA frequency band, which will allow us to combine our constraints on the RPL model with limits from Big Bang nucleosynthesis (BBN), the CMB, and LIGO–Virgo–KAGRA (LVK). Section 5, finally, contains our conclusion and a brief outlook on possible future applications of the RPL model.

2. Running Power Law

2.1. Spectral Model

The central observables in the context of PTA searches for GWs are the timing residuals R_a for a set of galactic millisecond pulsars. The imprint of a stochastic GWB on these timing residuals manifests itself in an extra contribution to the timing-residual cross-power spectrum for pairs of pulsars a and b (A. D. Johnson et al. 2024),

$$S_{ab}^{\rm GW}(f) = \Gamma_{ab}\,\frac{S_h(f)}{6\pi^2 f^2}. \tag{3}$$

Here, Γ_{ab} denotes the HD cross-correlation coefficients,

$$\Gamma_{ab}(\xi_{ab}) = (1 + \delta_{ab})\left[\frac{3}{2}\, x_{ab} \ln x_{ab} - \frac{x_{ab}}{4} + \frac{1}{2}\right], \tag{4}$$

with $x_{ab} = 1/2(1 - \cos \xi_{ab})$ and ξ_{ab} being the angular separation between pulsar a and pulsar b in the sky. S_h is the GW strain power spectrum, which is closely related to the characteristic GW strain amplitude,

$$h_c(f) = \sqrt{2f\, S_h(f)}, \tag{5}$$

as well as to the GW energy density spectrum in units of the critical energy density of the present Universe,

$$\Omega_{\rm GW}(f) = \frac{1}{\rho_{\rm crit}} \frac{d\rho_{\rm GW}(f)}{d \ln f} = \frac{4\pi^2}{3H_0^2} f^3\, S_h(f), \tag{6}$$

where $H_0 = 100\, h\, {\rm km\, s^{-1}\, Mpc^{-1}}$ is the Hubble constant and $h \sim 0.7$ (M. Kamionkowski & A. G. Riess 2023). Below, we will always work with $h^2\Omega_{\rm GW}$, which, unlike $\Omega_{\rm GW}$, is independent of the precise value of the Hubble constant.

The CPL model starts from a power-law ansatz for h_c,

$$h_c(f) \overset{\rm CPL}{=} A\left(\frac{f}{f_{\rm ref}}\right)^{\alpha}, \tag{7}$$

which immediately translates to a power law for $S_{ab}^{\rm GW}$,

$$S_{ab}^{\rm GW}(f) \overset{\rm CPL}{=} \Gamma_{ab}\, \frac{A^2}{12\pi^2 f_{\rm ref}^3}\left(\frac{f}{f_{\rm ref}}\right)^{-\gamma}, \tag{8}$$

with spectral index $\gamma = 3 - 2\alpha$, and similarly for $\Omega_{\rm GW}$,

$$\Omega_{\rm GW}(f) \overset{\rm CPL}{=} \frac{2\pi^2}{3H_0^2} A^2 f_{\rm ref}^2 \left(\frac{f}{f_{\rm ref}}\right)^{n}, \tag{9}$$

with spectral index $n = 5 - \gamma = 2\alpha + 2$. The relation in Equation (8) introduces the spectral index γ that we already referred to in Section 1. From this relation, $-\gamma$ can be identified with the coefficient of $x = \ln(f/f_{\rm ref})$ after taking the logarithm of both sides of the equation,

$$\ln S_{ab}^{\rm GW}(x) \overset{\rm CPL}{=} \ln\left(\Gamma_{ab}\, \frac{A^2}{12\pi^2 f_{\rm ref}^3}\right) - \gamma\, x, \tag{10}$$

which can also be written as

$$\gamma \overset{\rm CPL}{=} -\frac{\ln S_{ab}^{\rm GW}(x) - \ln S_{ab}^{\rm GW}(x=0)}{x}. \tag{11}$$

Alternatively, $-\gamma$ can be recovered from the derivative of the log of the timing-residual cross-power spectrum,

$$\gamma \overset{\rm CPL}{=} -\frac{d \ln S_{ab}^{\rm GW}}{dx}. \tag{12}$$

Both approaches yield, of course, the same result: the coefficient γ in front of the term linear in x in Equation (10) coincides with γ in Equation (12). To see this, simply differentiate both sides of Equation (10) with respect to x.

We shall now generalize the CPL model and allow for a running of the spectral index γ. To this end, we shall replace γ on the left-hand side of Equation (12) by our ansatz for the running spectral index $\gamma_{\rm run}$ in Equation (1), which yields a first-order differential equation for $S_{ab}^{\rm GW}$,

$$\gamma_{\rm run}(x) = \gamma + \beta\, x \overset{\rm RPL}{=} -\frac{d \ln S_{ab}^{\rm GW}}{dx}. \tag{13}$$

Then, imposing the same boundary condition as before,

$$S_{ab}^{\rm GW}(x=0) \overset{\rm RPL}{=} \Gamma_{ab}\, \frac{A^2}{12\pi^2 f_{\rm ref}^3}, \tag{14}$$

we can immediately write down the solution of Equation (13),

$$S_{ab}^{\rm GW}(f) \overset{\rm RPL}{=} \Gamma_{ab}\, \frac{A^2}{12\pi^2 f_{\rm ref}^3}\left(\frac{f}{f_{\rm ref}}\right)^{-\tilde{\gamma}_{\rm run}(f)}, \tag{15}$$

with the index $\tilde{\gamma}_{\rm run}$ in the exponent being given as

$$\tilde{\gamma}_{\rm run}(f) = \gamma + \frac{1}{2}\, \beta \ln\left(\frac{f}{f_{\rm ref}}\right). \tag{16}$$

Clearly, the two possible definitions of the spectral index that we encountered in Equations (11) and (12) now no longer agree, $\gamma_{\rm run} \neq \tilde{\gamma}_{\rm run}$. In this Letter, we will refer to $\gamma_{\rm run}$ as *the* running spectral index and $\tilde{\gamma}_{\rm run}$ as the *naive* running spectral index, because of the former's more useful geometric interpretation: in a plot with log–log axes, $-\gamma_{\rm run}$ directly measures the instantaneous slope of $S_{ab}^{\rm GW}(x)$ at x, while $-\tilde{\gamma}_{\rm run}$ measures the slope of the straight line connecting $S_{ab}^{\rm GW}(x)$ to $S_{ab}^{\rm GW}(x=0)$, which is of less interest in the RPL model. Both versions of the spectral index are related to each other via

$$\gamma_{\rm run}(x) = \frac{d}{dx}(\tilde{\gamma}_{\rm run}(x)x). \tag{17}$$

This relation is true in the RPL model, but it also holds in more general models for analogously defined indices $\gamma_{\rm run}$ and $\tilde{\gamma}_{\rm run}$ with arbitrary frequency dependence.

The relation in Equation (15) defines the RPL model at the level of the timing-residual cross-power spectrum. Similarly to the CPL model, we can express the information on the GWB also in terms of the characteristic GW strain amplitude

$$h_c(f) \overset{\rm RPL}{=} A\left(\frac{f}{f_{\rm ref}}\right)^{\tilde{\alpha}_{\rm run}(f)}, \tag{18}$$

with a naive running spectral index

$$\tilde{\alpha}_{\rm run}(f) = \frac{3}{2} - \frac{1}{2}\left[\gamma + \frac{1}{2}\, \beta \ln\left(\frac{f}{f_{\rm ref}}\right)\right], \tag{19}$$

as well as in terms of the GW energy density spectrum,

$$\Omega_{\rm GW}(f) \overset{\rm RPL}{=} \frac{2\pi^2}{3H_0^2} A^2 f_{\rm ref}^2 \left(\frac{f}{f_{\rm ref}}\right)^{\tilde{n}_{\rm run}(f)}, \tag{20}$$

with a naive running spectral index

$$\tilde{n}_{\rm run}(f) = 5 - \left[\gamma + \frac{1}{2}\, \beta \ln\left(\frac{f}{f_{\rm ref}}\right)\right]. \tag{21}$$

These results illustrate that the RPL model does indeed give rise to parabola-shaped GWB spectra; i.e., $\ln h^2\Omega_{\rm GW}$ is a second-order polynomial in $\ln f$,

$$\ln h^2\Omega_{\rm GW}(x) = c_0 + c_1\, x + \frac{1}{2}\, c_2\, x^2, \tag{22}$$

where $x = \ln(f/f_{\rm ref})$ as before and with coefficients

$$c_0 = \ln h^2\Omega_{\rm GW}|_{x=0} = \ln\left(\frac{2\pi^2}{3H_0^2}\, h^2A^2f_{\rm ref}^2\right), \tag{23}$$

$$c_1 = \left.\frac{d\ln h^2\Omega_{\rm GW}}{dx}\right|_{x=0} = 5 - \gamma, \tag{24}$$

$$c_2 = \left.\frac{d^2\ln h^2\Omega_{\rm GW}}{dx^2}\right|_{x=0} = -\beta. \tag{25}$$

The relation in Equation (24) illustrates that, up to a negative sign, the new parameter β can be interpreted as the curvature of the GWB spectrum on log–log axes, which agrees with the convention in I. Ben-Dayan et al. (2023). In the RPL model, this curvature is, in fact, constant, such that we do not have to restrict ourselves to $x = 0$:

$$\beta = -\frac{d^2\ln h^2\Omega_{\rm GW}}{dx^2} = \text{const.} \tag{26}$$

Here, the relative sign simply follows from the sign convention in Equation (15), according to which $S_{ab}^{\rm GW} \propto f^{-\tilde{\gamma}_{\rm run}}$.

2.2. Reference Frequency

Both the CPL model and the RPL model require one to specify a reference frequency $f_{\rm ref}$. This frequency, however, only serves as an auxiliary quantity and does not represent an independent physical parameter. In the CPL model, $f_{\rm ref}$ determines the physical meaning of the amplitude A: the value of the characteristic GW strain amplitude h_c at $f = f_{\rm ref}$. Meanwhile, γ is a constant and hence independent of the choice of $f_{\rm ref}$ in the CPL model. It is thus straightforward to translate any pair of values (A, γ) from one choice of $f_{\rm ref}$ to another,

$$\begin{pmatrix}\ln A'\\ \gamma'\end{pmatrix} \overset{\rm CPL}{=} \begin{pmatrix}1 & -\frac{R}{2}\\ 0 & 1\end{pmatrix}\begin{pmatrix}\ln A\\ \gamma\end{pmatrix} + \begin{pmatrix}\frac{3R}{2}\\ 0\end{pmatrix}, \tag{27}$$

where $R = \ln(f'/f_{\rm ref})$. The affine relation in Equation (27) expresses the simple idea that $\gamma' = \gamma$ and

$$A' \overset{\rm CPL}{=} A\left(\frac{f'}{f_{\rm ref}}\right)^{\alpha} \tag{28}$$

for any two choices of the reference frequency, $f_{\rm ref}$ and f', in the CPL model.

The situation in the RPL model is analogous. The choice of $f_{\rm ref}$ determines the physical meaning of A and γ: A is again the value of h_c at $f = f_{\rm ref}$, and $-\gamma$ is the spectral index of $S_{ab}^{\rm GW}$ at $f = f_{\rm ref}$. Meanwhile, the new parameter β is a constant and independent of $f_{\rm ref}$. Requiring the actual values of $S_{ab}^{\rm GW}$ to be invariant under a change of the reference frequency, $f_{\rm ref} \to f'$, we now obtain the following affine transformation,

$$\begin{pmatrix}\ln A'\\ \gamma'\\ \beta'\end{pmatrix} \overset{\rm RPL}{=} \begin{pmatrix}1 & -\frac{R}{2} & -\frac{R^2}{4}\\ 0 & 1 & R\\ 0 & 0 & 1\end{pmatrix}\begin{pmatrix}\ln A\\ \gamma\\ \beta\end{pmatrix} + \begin{pmatrix}\frac{3R}{2}\\ 0\\ 0\end{pmatrix}, \tag{29}$$

where the behavior of A reflects the idea that

$$A' \overset{\rm RPL}{=} A\left(\frac{f'}{f_{\rm ref}}\right)^{\tilde{\alpha}(f')}, \tag{30}$$

while the transformation behavior of γ amounts to

$$\gamma' \overset{\rm RPL}{=} \gamma_{\rm run}(f'), \tag{31}$$

in direct analogy to $\gamma = \gamma_{\rm run}(f_{\rm ref})$. Meanwhile, the running of the spectral index remains constant, $\beta' = \beta$.

Below, we will set $f_{\rm ref} = 1/10\,{\rm yr} \simeq 3.17\,{\rm nHz}$, which falls into the range of frequencies where NANOGrav's sensitivity to a GWB signal is maximal (see the NANOGrav sensitivity curve in G. Agazie et al. 2023f). This choice of reference frequency has the advantage that it helps to minimize the covariance among the parameters A, γ, and β in our Bayesian fit analysis. On the other hand, our choice of $f_{\rm ref}$ is still arbitrary, and it is an easy exercise to convert our result for the 3D posterior density of A, γ, and β that we will discuss in the next section to the posterior density at a different reference frequency.

Indeed, this conversion is straightforward at the level of the Markov Chain Monte Carlo (MCMC) that we obtain from our Bayesian fit analysis: to convert from $f_{\rm ref}$ to f', one simply has to apply Equation (29) to the MCMC on a sample-by-sample basis. In this way, one automatically accounts for the transformation behavior of the volume element in the 3D parameter space, which is crucial in order to correctly describe the transformation behavior of the posterior *density*. At the same time, we caution that Equation (29) cannot be used to convert marginalized 2D or 1D posterior densities from one choice of reference frequency to another, because marginalization and the transformation in Equation (29) do not commute. If one is interested in marginalized 2D or 1D posterior densities at a different reference frequency, one must first transform the full 3D posterior density according to Equation (29) and then marginalize, not vice versa.

3. Bayesian Fit to the NG15 Data

3.1. Tools and Methods

We now turn to our Bayesian fit of the RPL model to the NG15 data. Our analysis closely follows A. Afzal et al. (2023), where more details on the underlying formalism and conventions can be found. Similarly to A. Afzal et al. (2023), we use our software package `PTArcade` (A. Mitridate et al. 2023), a wrapper for `ENTERPRISE` (J. A. Ellis et al. 2019) and `ENTERPRISE_EXTENSIONS` (S. R. Taylor et al. 2021), to implement the RPL model and fit it to the NG15 data. `PTArcade` can be run in two different modes: "enterprise" and "ceffyl" (W. G. Lamb et al. 2023). We run it in "enterprise" mode, which means that we carry out a full Bayesian MCMC analysis in the time domain.

The different contributions to the NG15 timing residuals are treated in the same way as in A. Afzal et al. (2023): (i) all white-noise parameters are kept fixed at the maximum a posteriori (MAP) values recovered from single-pulsar analyses (G. Agazie et al. 2023f), (ii) linear offsets in the timing-ephemerides parameters are marginalized over, and (iii) pulsar-intrinsic red noise as well as the GWB signal are modeled using a discrete frequency basis $f_i = i/T$ (where $T \simeq 16.03$ yr is the total extent of the data set) in Fourier space. In addition to the linear offsets in the timing model, we also marginalize over the coefficients of this Fourier series, which results in the standard marginalized PTA likelihood (L. Lentati et al. 2013; R. van Haasteren & Y. Levin 2013). Meanwhile, we model pulse dispersion, again following A. Afzal et al. (2023), as a piecewise constant with the

Table 1
Prior Probability Density Distributions for the Free Parameters in Our Fit of the RPL Model to the NG15 Data

Parameter	Description	Prior	Comments
Pulsar-intrinsic red noise			
$A_{\rm red}$	Amplitude	Log-uniform $[-18, -12]$	One parameter per pulsar
$\gamma_{\rm red}$	Spectral index	Uniform [0, 10]	One parameter per pulsar
GWB in the RPL Model			
$A(1/10\ {\rm yr})$	Amplitude	Log-uniform $[-18, -12]$	One parameter per PTA
$\gamma(1/10\ {\rm yr})$	Spectral index	Uniform [0, 10]	One parameter per PTA
β	Running of the spectral index	Uniform $[-2, 4]$	One parameter per PTA

inclusion of DMX parameters (Z. Arzoumanian et al. 2015; M. L. Jones et al. 2017).

The only remaining free parameters in the marginalized likelihood are the parameters entering the covariance matrix of the time-correlated stochastic processes, i.e., pulsar-intrinsic red noise and the GWB signal. For each individual pulsar, we model red noise in terms of a power law with amplitude $A_{\rm red}$ and spectral index $\gamma_{\rm red}$, spanning from $f_1 = 1/T$ to $f_{30} = 30/T$. Meanwhile, the GWB signal is modeled in terms of the RPL expression for the timing-residual cross-power spectrum in Equation (15). As the GWB signal in the NG15 data mostly appears at lower frequencies, $f \lesssim f_{14} = 14/T$, we include the GWB contribution to the timing residuals only in the first 14 frequency bins. In total, this leaves us with 137 free parameters: $A_{\rm red}$ and $\gamma_{\rm red}$ for 67 pulsars plus the three free parameters of the RPL model, A, γ, and β. Each point in the space spanned by these 137 parameters defines a statistical ensemble of possible realizations of pulsar-intrinsic red noise and the GWB that all derive from the same covariance matrix but differ in terms of their explicit coefficients in Fourier space. The marginalized PTA likelihood no longer depends on these coefficients but serves as a likelihood on the 137-dimensional space of parameters (sometimes also called "hyperparameters") that control the power spectra of pulsar-intrinsic red noise and the GWB. In our Bayesian analysis, we sample from the posterior density of our 137 model parameters using MCMC techniques (J. Ellis & R. van Haasteren 2017) applied to the marginalized PTA likelihood and the prior densities summarized in Table 1. Our priors are agnostic about the source of the GWB signal and large enough so that they can accommodate the entire 3D 95% posterior volume of the RPL model. Our final MCMC chain encompasses nearly 3 million samples and is composed of 20 independent subchains.

The CPL model can be fitted to the NG15 data in the same way as the RPL model, the only difference being that β needs to be set to $\beta = 0$ at all times. We make use of this fact and employ product-space methods (B. P. Carlin & S. Chib 1995; S. J. Godsill 2001; S. Hee et al. 2015) to fit both models simultaneously and thus determine the Bayes factor $\mathcal{B}$ for the RPL-versus-CPL model comparison. In fact, we use statistical bootstrapping methods to determine a mean value and a standard deviation for the Bayes factor (B. Efron & R. Tibshirani 1986; see the discussion in A. Afzal et al. 2023 for more details).

Before we turn to the discussion of our results, let us also briefly compare our analysis to one in I. Ben-Dayan et al. (2023). While we work with the marginalized PTA likelihood for the NG15 timing residuals, I. Ben-Dayan et al. (2023) start from the 2D posterior density for A and γ in the CPL model. They extract this posterior density from G. Agazie et al. (2023a), reinterpret it as a likelihood, and then use this likelihood to fit various GWB models, including a modification of the RPL model that also accounts for the dynamics of reheating after inflation. That is, they refit an RPL-like model to the 2D posterior density of the CPL model, which provides them with tight bounds on $c_2 = -\beta$ in Equation (24), $|c_2| \lesssim 0.12$. As we will now discuss, our analysis results in less tight bounds on β, as we do not start from the 2D posterior density of the CPL model but rather allow our MCMC sampler to explore the whole 3D parameter space of the RPL model subject to the priors in Table 1.

3.2. Results

The main result of our Bayesian fit analysis is the 3D posterior density for the RPL parameters A, γ, and β. The marginalized 2D and 1D posterior densities that can be derived from this 3D density are shown in the corner plot in Figure 1. In one, two, and three dimensions, we rely on kernel density estimation (KDE; specifically, the `GetDist` package; A. Lewis 2019) in order to construct smooth densities from discrete sets of MCMC samples.

The KDE approximation of the 3D posterior density allows us to determine the MAP point in parameter space, i.e., the point of highest 3D posterior density. We list the coordinates of this point in the second column of Table 2 and mark its position in Figure 1 with an orange colored plus sign. Similarly, we can derive point and interval estimates from the three marginalized 1D posterior densities shown in Figure 1. Specifically, we determine the MAP values of A, γ, and β according to their respective 1D densities (see the third column in Table 2) and the corresponding 68% and 95% credible intervals (see the fourth and fifth columns in Table 2). Here, the credible intervals are defined as highest-posterior-density intervals (HPDIs); i.e., we integrate the 1D densities over regions of highest posterior density until the integral returns an integrated probability of 68% or 95%.

Based on the values listed in Table 2, we are unable to claim evidence for nonzero running of the spectral index in the PTA frequency band; our Bayesian interval estimates for β are perfectly consistent with the assumption of no running, $\beta = 0$. Conversely, there is nothing wrong with assuming nonzero running. In fact, our results indicate that β can easily be of $\mathcal{O}(1)$. The 68% credible interval for β even barely includes $\beta = 0$, and the 3D and 1D MAP values of β are clearly nonzero. We therefore conclude that, while the NG15 data do not yet suffice to claim the discovery of nonzero β, future PTA data sets may well enable such a measurement.

Besides parameter inference, we are also interested in exploring the implications of our analysis for the GWB spectrum. We do this in two different ways.

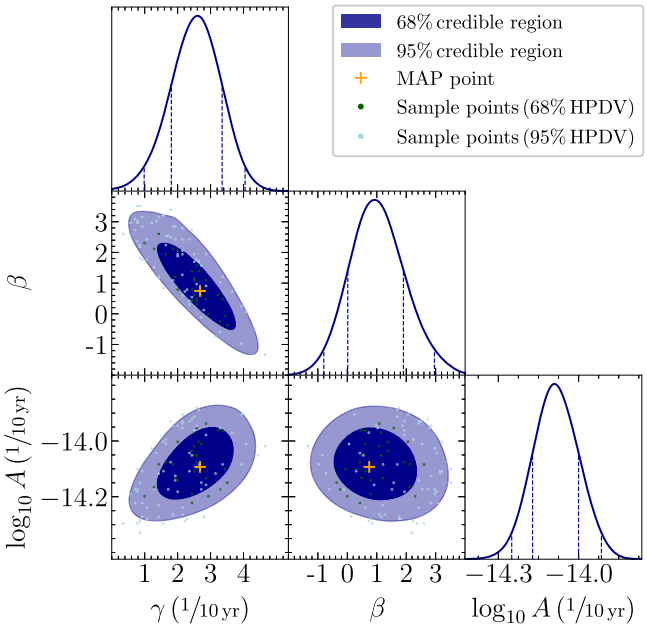

Figure 1. Corner plot of the 3D parameter space of the RPL model. The blue shaded regions in the off-diagonal plots and the solid blue curves in the diagonal plots show the marginalized 2D and 1D posterior densities for the RPL model parameters, respectively. The dark blue regions mark 68% credible regions, the light blue regions mark 95% credible regions, and the dashed vertical lines mark 68% and 95% credible intervals. The cyan and green colored points represent random samples from the 68% and 95% HPDVs in the 3D parameter space, respectively. The orange plus sign marks the point where the 3D posterior density reaches its maximum (see the second column in Table 2). The GWB spectra corresponding to the colored points are shown in identical colors in Figure 2.

Table 2
Point and Interval Estimates for the Parameters of the RPL Model

Parameter	3D MAP Value	1D MAP Value	68% Credible Interval	95% Credible Interval
$\log_{10}A(1/10\,\mathrm{yr})$	−14.09	−14.09	[−14.17, −14.00]	[−14.25, −13.91]
$\gamma(1/10\,\mathrm{yr})$	2.68	2.60	[1.81, 3.35]	[0.98, 4.05]
β	0.74	0.92	[0.01, 1.90]	[−0.80, 2.96]

Note. The second column states the MAP value for each parameter based on the full 3D posterior density. The third through fifth columns state the MAP values and HPDIs at the 68% and 95% credible level based on the three marginalized 1D posterior densities in Figure 1.

(1) *Bayesian credible bands.* In Figure 2, we show what we shall refer to as 68% and 95% credible bands for the GWB spectrum predicted by the RPL model. These bands are based on the 68% and 95% highest-posterior-density volumes (HPDVs) in the 3D parameter space. In fact, they can be regarded as the projection of these HPDVs onto the space of possible GWB spectra. In order to construct the HPDVs in the 3D parameter space, we proceed in the same way as for the HPDIs in the marginalized 1D posterior densities: we integrate the KDE approximation of the 3D density over regions of highest posterior density until the integral returns an integrated probability of 68% or 95%. In the next step, we then take all points inside these HPDVs, compute the GWB spectra that they predict, and draw all these spectra in a plot of $h^2\Omega_{\mathrm{GW}}$ as a function of f. This procedure results in two families of GWB spectra (spectra belonging to points in the 68% HPDV and

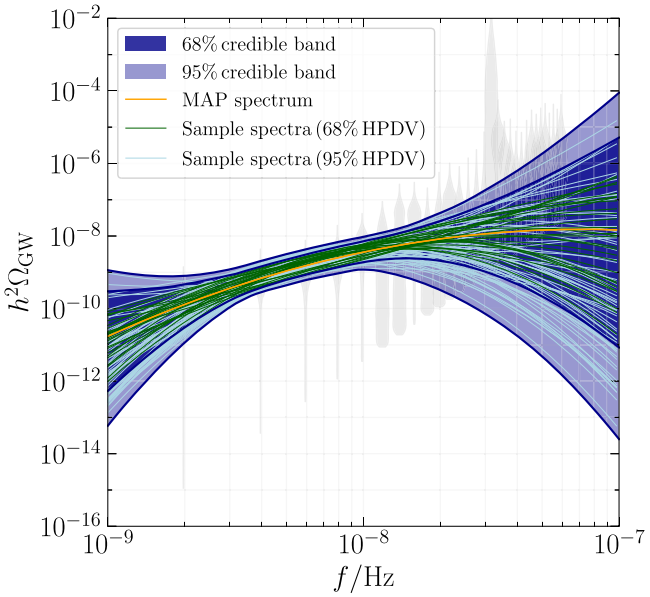

Figure 2. GWB spectra predicted by the RPL model. The blue shaded bands encompass all spectra that are associated with points inside the 68% and 95% HPDVs in the 3D parameter space. The cyan, green, and orange colored spectra belong to the parameter points shown in Figure 1. The gray "violins" in the background represent the posterior densities for the 30 values of the GW energy density spectrum, $\{h^2\Omega_{\mathrm{GW}}(f_i)\}$ with $f_i = i/T$ and $i = 1 \cdots 30$, in the free spectral model.

spectra belonging to points in the 95% HPDVs). The envelopes of these two families of GWB spectra define the 68% and 95% credible bands shown in Figure 2. In order to illustrate the algorithm behind this construction, we show a handful of sample points in the 68% or 95% HPDVs in Figure 1 and their associated GWB spectra in identical colors in Figure 2. In the limit of a large number of samples in Figure 1, the sample spectra in Figure 2 begin to shape out the 68% and 95% credible bands. On top, we show the position of the 3D MAP point in Figure 1 and the GWB spectrum that it predicts in Figure 2.

(2) *Bayesian periodogram.* In Figure 3, we present the Bayesian periodogram for the RPL model and compare it to the Bayesian periodogram for the free spectral model. Both periodograms display the posterior densities for the 14 values of the GW energy density spectrum, $\{h^2\Omega_{\mathrm{GW}}(f_i)\}$, at $f_i = i/T$ with $i = 1 \cdots 14$. Given a large number of MCMC samples, these posterior densities can be simply constructed from histograms of $h^2\Omega_{\mathrm{GW}}(f_i)$ values (i.e., one histogram at each frequency f_i), in combination with a KDE approximation. Specifically, in order to create the periodograms in Figure 3, we used tools included in NANOGrav's `holodeck` software package (G. Agazie et al. 2023c). The periodogram of the free spectral model corresponds to what is better known as the NG15 "violins"; these "violins" (in their complete, two-sided form) are also shown in gray in Figure 2. Similarly, the periodogram of the RPL model may be referred to as the "RPL violins." Based on the periodogram of the RPL model, one could in principle construct what we referred to as the "median GWB spectrum" in A. Afzal et al. (2023): a curve that connects the median of the first RPL violin with the median of the second RPL violin, and so on. However, a potentially misleading issue related to the concept of median GWB spectra is that they almost never coincide with an individual GWB spectrum at a certain point in the model parameter space.

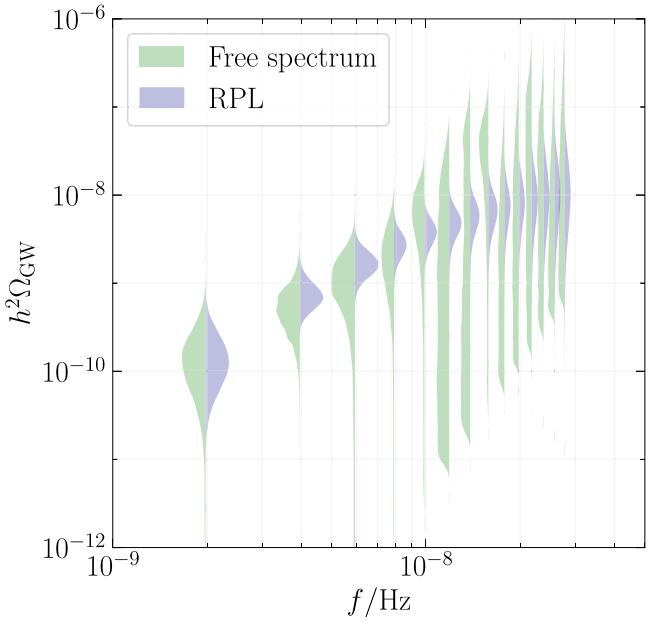

Figure 3. Bayesian periodograms for the free spectral model (green "violins") and the RPL model (purple "violins"). Each "half-violin" corresponds to a Bayesian posterior probability density for the respective value of $h^2\Omega_{\rm GW}(f_i)$.

In the case of the RPL model, this means that its median GWB spectrum would not exactly correspond to a parabola, even though every single individual GWB spectrum predicted by the RPL model is parabola-shaped. We therefore refrain from showing the median GWB spectrum of the RPL model and only present its periodogram, which in any case contains more information than just the median GWB spectrum by itself. Meanwhile, explicit GWB spectra that are predicted by the RPL model are shown in Figure 2.

The plots in Figures 2 and 3 contain complementary information. To see this, first note that the Bayesian periodogram in Figure 3 results in 68% and 95% credible intervals for the values of $h^2\Omega_{\rm GW}(f_i)$ in each frequency bin f_i. These intervals, however, do not exactly coincide with the extent of the 68% and 95% credible bands in Figure 2. The 95% band in Figure 2, e.g., is constructed from the 95% of all MCMC samples that lie closest together in the parameter region of highest 3D posterior density. The 95% intervals in Figure 3, on the other hand, belong to the 95% of all MCMC samples whose values of $h^2\Omega_{\rm GW}(f_i)$ lie closest together (but whose parameter points may not necessarily lie close together). This means that, in both cases, 95% of all MCMC samples are used—but not exactly the same selection.

As a consequence, the plots in Figures 2 and 3 provide answers to two slightly different questions. The Bayesian credible bands in Figure 2 better reflect the perspective of a model-building theorist who works under the assumption that the GWB signal is caused by a physical mechanism that indeed results in an RPL spectrum and that determines the true, physical values of A, γ, and β. If these physical values should correspond to the 3D MAP point in Figure 1, the MAP spectrum in Figure 2 will be realized; if the physical values should slightly deviate from the 3D MAP point, the spectrum will slightly deviate from the MAP spectrum, and so on. In this sense, the credible bands in Figure 2 tell us in which range we should expect the true spectrum to fall if we believe that the underlying mechanism singles out a specific region of parameter space. The Bayesian periodogram in Figure 3, on the other hand, remains ignorant toward the physical meaning of A, γ, and β. It better reflects the perspective of a theory-agnostic experimentalist who is primarily interested in the spectral shape of the GWB signal. From the periodogram, the experimentalist can read off in what proportion certain values of $h^2\Omega_{\rm GW}(f_i)$ are realized across all MCMC samples, independent of the precise values of A, γ, and β that are needed to obtain these values of $h^2\Omega_{\rm GW}(f_i)$. In short, the credible bands in Figure 2 group together our MCMC samples according to their A, γ, and β values; the periodogram in Figure 3 groups together our MCMC samples according to the shape of the GWB spectrum.

The main message from both Figures 2 and 3 is that the RPL model provides a good fit of the NG15 data that is consistent with the free spectral reconstruction. Moreover, both figures yield an impression of how the "violins" of the free spectral reconstruction are probably going to evolve with more data in the future, if the GWB spectrum should indeed have an RPL-like shape.

We conclude our discussion by quoting the Bayes factor for the RPL-versus-CPL model comparison that we obtain from the hypermodel run described in Section 3.1,

$$\mathcal{B}(\text{RPL versus CPL}) = 0.69 \pm 0.01. \tag{32}$$

This value is inconclusive and indicates neither a preference for nor a rejection of the RPL model in comparison to the CPL model. The fact that $\mathcal{B}$ is slightly less than unity can in particular be attributed to the larger dimensionality of the RPL parameter space: compared to the CPL model, the RPL model does not significantly improve the quality of the fit of the NG15 data. At the same time, the RPL model features one parameter more than the CPL model, which results in a larger prior volume and hence a slight suppression of the Bayes factor. In view of these results, we conclude that, at present, the CPL model still suffices to adequately describe the NANOGrav signal. Given the results in Table 2, it is, however, conceivable that future PTA data sets may well lead to a measurement of nonzero running. With a bit of luck, β may even turn out to be of $\mathcal{O}(1)$, which would be instrumental in the context of model selection.

4. Inflationary Gravitational Waves

Thus far, we only used the RPL model to describe the GWB signal in the PTA frequency band. It is, however, interesting to ask whether the RPL model is also capable of describing a GWB signal extending over a larger frequency range. In the extreme case, one could imagine an RPL-like signal reaching from ultralow frequencies, $f \sim 10^{-(17\cdots16)}$ Hz, which are probed in CMB observations, to high frequencies, $f \sim 10^{2\cdots3}$ Hz, which are probed in terrestrial GW interferometer experiments. The physical origin of such a broadband GWB signal would necessarily be primordial. In fact, an RPL-like signal stretching over 20 orders of magnitude in frequency space could originate from cosmic inflation (M. C. Guzzetti et al. 2016), the stage of accelerated expansion prior to the Hot Big Bang (i.e., the radiation-dominated era in the early Universe). Cosmic inflation stretches primordial scalar and tensor perturbations to superhorizon scales, where they freeze out, before they eventually become dynamical again upon horizon reentry during radiation domination. Primordial scalar perturbations reenter the horizon in the form of density perturbations of the

primordial plasma, while primordial tensor perturbations turn into propagating GWs upon horizon reentry. We shall refer to the GWB signal thus produced by inflation as inflationary GWs (IGWs; L. P. Grishchuk 1974; A. A. Starobinsky 1979; V. A. Rubakov et al. 1982; R. Fabbri & M. d. Pollock 1983; L. F. Abbott & M. B. Wise 1984).

4.1. Upper Limits

In this section, we will interpret the RPL model as an approximate phenomenological description of IGWs, which will allow us to supplement the results from our Bayesian fit analysis in the previous section with several observational bounds at lower and higher frequencies. For related earlier work that also interprets the PTA signal in terms of IGWs, see S. Kuroyanagi et al. (2021), S. Vagnozzi (2021, 2023), and M. Benetti et al. (2022). However, all of these analyses model the IGW spectrum either in terms of a CPL, a broken power law, or a piecewise power law (in order to account for the possibility of late-time entropy production). The present Letter is the first one to consider an RPL-type signal as a simplified model for an IGW spectrum that is also capable of explaining the NANOGrav signal. In total, we are interested in three upper limits on IGWs.

(1) *Tensor-to-scalar ratio*. Assuming the RPL-like signal extends from PTA frequencies all the way to CMB frequencies, we must ensure that we do not violate the upper limit on the tensor-to-scalar ratio, i.e., the ratio of the primordial tensor and scalar amplitudes, $r = A_t/A_s$. In order to translate this bound to a constraint on the RPL parameters, we must first map the IGW spectrum onto the RPL model. The GWB spectrum predicted by inflation reads (C. Caprini & D. G. Figueroa 2018)

$$h^2\Omega_{\rm IGW}(f) = \frac{h^2\Omega_{\rm rad}^0}{24}\,\mathcal{G}(f)\mathcal{T}(f)\mathcal{P}_t(f). \tag{33}$$

Here, $h^2\Omega_{\rm rad}^0 \simeq 4.2 \times 10^{-5}$ is the present-day value of the radiation energy density (assuming three relativistic neutrino species) in units of the critical energy density times the dimensionless Hubble constant h squared.

The function $\mathcal{G}$ accounts for the varying number of degrees of freedom during the cosmic expansion history,

$$\mathcal{G}(f) = \left(\frac{g_*(f)}{g_*^0}\right)\left(\frac{g_{*,s}^0}{g_{*,s}(f)}\right)^{4/3}, \tag{34}$$

where g_* and $g_{*,s}$ are the effective numbers of relativistic degrees of freedom entering the radiation energy density $\rho_{\rm rad}$ and radiation entropy density $s_{\rm rad}$, respectively,

$$\rho_{\rm rad} = \frac{\pi^2}{30}\,g_*\,T^4, \qquad s_{\rm rad} = \frac{2\pi^2}{45}\,g_{*,s}\,T^3. \tag{35}$$

In order to evaluate these two relations precisely, several effects have to be taken account (K. Saikawa & S. Shirai 2018, 2020), including different quantum statistics for fermions and bosons as well as various perturbative and nonperturbative corrections, which explains why g_* and $g_{*,s}$ typically assume noninteger values. In Equation (34), $g_*^0 \simeq 3.38$ and $g_{*,s}^0 \simeq 3.93$ denote the present-day values of these two quantities (assuming three relativistic neutrino species), while $g_*(f)$ and $g_{*,s}(f)$ represent the values of these two quantities in the early Universe when the IGW mode with present-day frequency f and comoving wavenumber k reentered the Hubble radius, $k = aH$ (with scale factor a and Hubble rate H).

The function $\mathcal{T}$ is a transfer function that accounts for the transition from radiation to matter domination,

$$\mathcal{T}(f) = 1 + \frac{9}{16}\left(\frac{f_{\rm eq}}{\sqrt{2}\,f}\right)^2, \tag{36}$$

where $f_{\rm eq} \simeq 2.1 \times 10^{-17}$ Hz is the present-day frequency of the IGW mode that reentered the horizon at the time of matter–radiation equality. Finally, the last factor in Equation (33) is the primordial tensor power spectrum, which describes the strength of GW production during inflation as a function of f. We shall assume that inflation gives rise to an RPL-like spectrum of IGWs, such that

$$\mathcal{P}_t(f) = r\,A_s\left(\frac{f}{f_{\rm CMB}}\right)^{n_t + 1/2\,\beta_t \ln(f/f_{\rm CMB})}, \tag{37}$$

with a tensor-to-scalar ratio r, primordial scalar amplitude $A_s \simeq 2.1 \times 10^{-9}$, primordial tensor index n_t, running of the primordial tensor index β_t, and CMB pivot frequency $f_{\rm CMB} = 0.05\,{\rm Mpc}^{-1}/(2\pi) \simeq 7.7 \times 10^{-17}$ Hz.

At the lowest order in the slow-roll parameters, standard single-field slow-roll inflation predicts a consistency relation between the tensor-to-scalar ratio and the primordial tensor index, $n_t = -r/8$ (A. R. Liddle & D. H. Lyth 2000), which implies that n_t must be negative. A red-tilted IGW spectrum (i.e., $h^2\Omega_{\rm IGW}$ with $n_t < 0$), however, has no chance of explaining the signal in the PTA band. An important assumption underlying our analysis therefore is that the dynamics of inflation are nonminimal (possibly involving several scalar fields or other particle degrees of freedom), such that the consistency relation $n_t = -r/8$ can be circumvented and a blue-tilted IGW spectrum (i.e., $h^2\Omega_{\rm IGW}$ with $n_t > 0$) is realized. Of course, such a *blue*-tilted signal will still appear as correlated common *red* noise (i.e., $\gamma > 0$) in PTA data, unless n_t is unrealistically large (see Equation (40) below).

In addition to the factors shown in Equation (33), we could in principle add another factor, i.e., an additional transfer function $\mathcal{T}_{\rm rh}$ accounting for the transition from reheating to radiation domination. In fact, in A. Afzal et al. (2023), we included precisely such a transfer function. However, in the present Letter, we will ignore the dynamics of reheating and simply work with the GWB spectrum in Equation (33) for two reasons. First, the dynamics of reheating are model-dependent and introduce at least three more parameters: the reheating temperature, $T_{\rm rh}$; the equation-of-state parameter during reheating, $w_{\rm rh}$; and the duration of reheating measured in e-folds, $N_{\rm rh}$. Second, $\mathcal{T}_{\rm rh}$ only becomes relevant at very high frequencies or for low values of the reheating temperature. Our decision to neglect $\mathcal{T}_{\rm rh}$ thus amounts to the assumption of a high reheating temperature such that $\mathcal{T}_{\rm rh}$ remains irrelevant all the way up to LVK frequencies.

With Equation (33) at our disposal, we are now ready to match the IGW spectrum to the RPL model in the PTA band. All frequencies in the PTA band are clearly much larger than $f_{\rm eq}$ in Equation (36), which allows us to set $\mathcal{T} = 1$ in our matching procedure. Furthermore, we note that the frequency dependence encoded in $\mathcal{G}$ cannot be captured by the RPL model. This is, however, not a big issue, as $\mathcal{G}$ only varies

between $\mathcal{G} = 1$ at low frequencies and $\mathcal{G} \simeq 0.39$ at high frequencies in any case. For the purposes of a rough matching between the IGW and RPL models, it is therefore justified to set $\mathcal{G} = 1$ as well. This leaves us with the simple matching condition

$$\frac{\Omega_{\rm rad}^0}{24}\,\mathcal{P}_t(f) \approx \frac{2\pi^2}{3H_0^2}\,A^2 f_{\rm ref}^2 \left(\frac{f}{f_{\rm ref}}\right)^{\tilde{n}_{\rm run}(f)} \tag{38}$$

for frequencies f in the PTA band. Both sides of this condition describe parabola-shaped GWB spectra (if plotted on log–log axes), which allows us to derive a unique solution for the IGW parameters,

$$r = \frac{24}{\Omega_{\rm rad}^0}\frac{1}{A_s}\frac{2\pi^2}{3H_0^2}\,A^2 f_{\rm ref}^2 \left(\frac{f_{\rm CMB}}{f_{\rm ref}}\right)^{\tilde{n}_{\rm run}(f_{\rm CMB})}, \tag{39}$$

$$n_t = 5 - \gamma - \beta \ln\left(\frac{f_{\rm CMB}}{f_{\rm ref}}\right), \qquad \beta_t = -\beta. \tag{40}$$

We can also think of the matching of the IGW and RPL models as a change of reference frequency, $f_{\rm CMB} \to f_{\rm ref}$, keeping in mind that $\mathcal{T} \to 1$ as we move up in frequency space. From this perspective, the relations in Equations (39) and (40) can be understood as a direct consequence of the transformation law in Equation (29).

At present, no reliable bounds on n_t, let alone β_t, exist. We therefore only work with the current upper limit on the tensor-to-scalar ratio based on the latest PLANCK and BICEP/Keck data, $r \lesssim 0.03$ at 95% confidence level (M. Tristram et al. 2022; G.-Galloni et al. 2024), which implies

$$h^2\Omega_{\rm GW}(f_{\rm CMB}) \lesssim 1.1 \times 10^{-16}\left(\frac{r}{0.03}\right). \tag{41}$$

This inequality represents the most compact way of writing the constraint on the RPL parameters that follows from the upper limit on r. At the same time, it is important to note that, in scenarios where the signal in the PTA band indeed corresponds to an RPL-like spectrum of inflationary origin, the actual, physical amplitude of the GWB spectrum at $f_{\rm CMB}$ is given by $h^2\Omega_{\rm IGW}(f_{\rm CMB})$ (see Equation (33)), including the transfer function $\mathcal{T}$, and not by $h^2\Omega_{\rm GW}(f_{\rm CMB})$ in the RPL model (see Equation (20)). The numerical difference between both values is small, but the conceptual difference is worth paying attention to.

(2) *Dark radiation.* A primordial GWB from inflation contributes to the energy density of dark radiation (i.e., additional relativistic degrees of freedom beyond the photon and the three Standard Model neutrino species) at the time of BBN. Requiring dark radiation not to spoil the successful BBN prediction of the primordial abundances of the light elements thus puts an upper limit on the integrated energy density of IGWs. This limit can be expressed in terms of $N_{\rm eff}$, the effective number of relativistic neutrino species in the early Universe, or, more precisely, $\Delta N_{\rm eff}$, the deviation of $N_{\rm eff}$ from its Standard Model value (M. Drewes et al. 2024),

$$\Delta N_{\rm eff} = N_{\rm eff} - N_{\rm eff}^{\rm SM}, \qquad N_{\rm eff}^{\rm SM} \simeq 3.0440. \tag{42}$$

With this notation, the dark-radiation bound on the IGW energy density reads (C. Caprini & D. G. Figueroa 2018)

$$\int_{f_{\rm BBN}}^{f_{\rm end}} \frac{df}{f}\, h^2\Omega_{\rm GW}(f) \lesssim 5.6 \times 10^{-6}\Delta N_{\rm eff}. \tag{43}$$

Here, $f_{\rm BBN}$ is the present-day frequency of the IGW mode that reentered the horizon at the onset of BBN at temperatures $T \sim 0.1$ MeV. For definiteness, we will set $f_{\rm BBN} = 10^{-12}$ Hz in what follows. Similarly, $f_{\rm end}$ denotes the present-day frequency of the IGW mode that was just as large as the horizon at the end of inflation. The precise value of $f_{\rm end}$ depends on the dynamics of reheating, in particular, $T_{\rm rh}$, $w_{\rm rh}$, and $N_{\rm rh}$. For large values of the reheating temperature and in the relevant part of the RPL parameter space, the integral over the GW energy density spectrum, however, becomes insensitive to the exact choice of the upper integration boundary. In our analysis, we especially assume that the RPL-like shape of the spectrum persists at least up to the LVK frequency band, which translates to $T_{\rm rh} \gtrsim 10^{10}$ GeV (K. Nakayama et al. 2008). For such large values of $T_{\rm rh}$, we find that the integral over $h^2\Omega_{\rm GW}$ is independent of the exact value of $f_{\rm end}$ to very good approximation. The reason for this is that, for large $f_{\rm end}$ and RPL parameter values satisfying the bound in Equation (43), the bulk contribution from the integrand to the total integral is simply located at frequencies $f \ll f_{\rm end}$, such that variations in $f_{\rm end}$ have no numerical impact.

Pictorially speaking, we can say that the RPL spectrum bends away toward smaller values of $h^2\Omega_{\rm GW}$ long before it reaches $f_{\rm end}$. In our numerical analysis, we set $f_{\rm end} = 10^4$ Hz, for definiteness, and neglect any possible effect of reheating on the shape of the spectrum (see our above comment on the transfer function for the transition from reheating to radiation domination). Moreover, because of the strong suppression of the RPL spectrum as it approaches its endpoint at $f_{\rm end}$ (for parameter values satisfying the bound in Equation (43)), we conclude that our analysis is less sensitive to possible corrections to the slow-roll dynamics of the inflaton field toward the end of inflation (W. H. Kinney 2021). In fact, assuming a large $T_{\rm rh}$, all relevant frequency scales in our analysis, $f_{\rm CMB}$, $f_{\rm BBN}$, $f_{\rm ref}$, and $f_{\rm LVK}$, correspond to IGW modes that exit the horizon long before the end of inflation.

The upper limit on $\Delta N_{\rm eff}$ depends on the choice of cosmological model and combination of data sets. The amount of dark radiation in the early Universe can notably also be constrained by CMB observations, next to the primordial abundances of the light elements. PLANCK data alone yield an upper limit at 95% confidence level of around $\Delta N_{\rm eff} \lesssim 0.3$ (N. Aghanim 2020), with the exact value depending on the choice of model fitted to the PLANCK data. However, combining BBN and CMB data, one has to deal with a larger range of uncertainties, which slightly weakens the upper limit (O. Pisanti et al. 2021; T.-H. Yeh et al. 2021). In our analysis, we will hence work with a more conservative bound, $\Delta N_{\rm eff} \lesssim 0.5$.

Before we move on to our third and final parameter constraint, we mention in passing that the integral in Equation (43) can be solved analytically in the RPL model,

$$h^2\Omega_{\rm GW}^{\rm tot} = \frac{2\pi^2}{3H_0^2}\,h^2A^2f_{\rm ref}^2\,\sqrt{\frac{\pi}{2\beta}}\,e^{\frac{(-5+\gamma)^2}{2\beta}}\,E_{x_{\rm BBN}}^{x_{\rm end}}, \tag{44}$$

where we introduced the shorthand notation

$$E_{x_{\rm BBN}}^{x_{\rm end}} = \mathrm{erf}\left(\frac{-5+\gamma+\beta\, x}{\sqrt{2\beta}}\right)\Bigg|_{x_{\rm BBN}}^{x_{\rm end}}. \tag{45}$$

Here, erf denotes the Gauss error function and $x_{\rm BBN} = \ln(f_{\rm BBN}/f_{\rm ref})$ and $x_{\rm end} = \ln(f_{\rm end}/f_{\rm ref})$. This analytical expression comes in handy, e.g., when one is interested in varying the integration boundaries $f_{\rm BBN}$ and $f_{\rm end}$ without redoing the whole integral. Note that, despite the factors of $\sqrt{\beta}$, the formula for $h^2\Omega_{\rm GW}^{\rm tot}$ in Equation (44) is actually also valid for $\beta < 0$. In this case, all imaginary contributions cancel out, and the overall result ends up being real and positive, as it should be. Moreover, the expression in Equation (44) also reproduces the correct limit for the case of no running, i.e., the CPL model,

$$\lim_{\beta\to 0} h^2\Omega_{\rm GW}^{\rm tot} = \frac{2\pi^2}{3H_0^2}\, h^2A^2 f_{\rm ref}^2\, \frac{(f/f_{\rm ref})^{5-\gamma}}{5-\gamma}\Bigg|_{f_{\rm BBN}}^{f_{\rm end}}, \tag{46}$$

as well as the correct limit for a flat GWB spectrum,

$$\lim_{\substack{\beta\to 0\\ \gamma\to 5}} h^2\Omega_{\rm GW}^{\rm tot} = \frac{2\pi^2}{3H_0^2}\, h^2A^2 f_{\rm ref}^2\, \ln\left(\frac{f_{\rm end}}{f_{\rm BBN}}\right). \tag{47}$$

(3) *GWB amplitude at LVK frequencies.* Finally, we require the RPL-like signal from inflation not to violate the upper limit on the amplitude of the stochastic GWB at LVK frequencies (R. Abbott et al. 2021):

$$\Omega_{\rm GW}(f_{\rm LVK}) \lesssim 1.7\times 10^{-8}, \qquad f_{\rm LVK} = 25\ \mathrm{Hz}. \tag{48}$$

In the derivation of this limit, the LVK Collaboration set the dimensionless Hubble constant to $h = 0.679$, which implies the following constraint on $h^2\Omega_{\rm GW}$:

$$h^2\Omega_{\rm GW}(f_{\rm LVK}) \lesssim 7.8\times 10^{-9}. \tag{49}$$

4.2. Discussion

In total, we have now derived three constraints on the RPL parameter space (see Equations (41), (43), and (49)). In Figure 4, we show the three bounds on β in dependence of γ and for fixed A that result from these constraints. $\log_{10}A$ is fixed at its MAP value, $\log_{10}A = -14.09$ (see Table 2), in Figure 4, which is justified by the fact that our fit of the RPL model to the NG15 data returns a very narrow credible interval for $\log_{10}A$. That is, $\log_{10}A$ is well constrained by the data, which allows us to reduce our discussion of parameter bounds from a 3D problem to a 2D problem. On top, we observe that the CMB and LVK bounds in Figure 4 exhibit only a very weak, logarithmic dependence on A. Even if we vary A by several orders of magnitude around the value chosen in Figure 4, we obtain nearly identical results for the bounds in the γ–β plane in Figure 4, which illustrates the weak sensitivity of our results to uncertainties in the IGW model. The weak, logarithmic dependence of the CMB and LVK bounds on A is a consequence of the large distances on the frequency axis involved in the problem: if we intend to preserve a certain value of $h^2\Omega_{\rm GW}$ at $f = f_{\rm CMB}$ or $f = f_{\rm LVK}$, even a large variation of A at $f = f_{\rm ref}$ can be easily compensated for by a small shift in β. In short, because of the large hierarchy $f_{\rm CMB} \ll f_{\rm ref} \ll f_{\rm LVK}$, small changes in β have a large leverage effect.

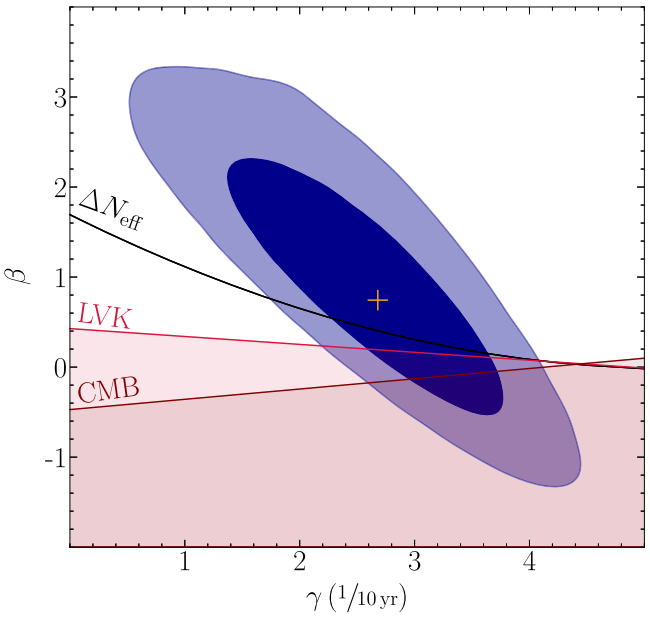

Figure 4. Bounds on the RPL parameters β and γ in scenarios where the NANOGrav signal is identified with an RPL-like signal of inflationary origin. The bounds labeled CMB, $\Delta N_{\rm eff}$, and LVK are derived from the upper limits on the (i) tensor-to-scalar ratio, (ii) amount of dark radiation, and (iii) GWB amplitude at LVK frequencies, respectively. Parameter values below any of the three solid lines are excluded.

This argument does not apply to the $\Delta N_{\rm eff}$ bound, which is not a constraint on a local value of the GWB spectrum but a global constraint on the integral of the GWB spectrum. Correspondingly, the $\Delta N_{\rm eff}$ is more sensitive to variations of A. On the other hand, because of the narrow credible interval for $\log_{10}A$, we are less interested in the behavior of the $\Delta N_{\rm eff}$ bound at $\log_{10}A \gg -14$ or $\log_{10}A \ll -14$. In any case, it would be straightforward to study the A dependence of the $\Delta N_{\rm eff}$ bound using the expressions in Equations (44) and (45).

As evident from Figure 4, large regions of the RPL parameter space that can account for the NANOGrav signal are consistent with all three bounds discussed in Section 4.1. We therefore conclude that a parabola-shaped GWB spectrum of inflationary origin and extending over 20 orders of magnitude in frequency space is indeed a viable option. The fact that only positive values of β are in accord with all three bounds in Figure 4 tells us in particular that this GWB spectrum needs to be negatively curved. That is, while $h^2\Omega_{\rm GW}$ must be an increasing function of frequency in the PTA band (i.e., $\gamma < 5$), the spectrum must eventually bend away toward smaller values again when moving up along the frequency axis, in order to satisfy the $\Delta N_{\rm eff}$ and LVK bounds. Interestingly enough, the CMB bound derived from the upper limit on the tensor-to-scalar ratio actually also allows for positively curved parabolas (i.e., $\beta < 0$, which means $\beta_t > 0$; see Equation (40)). For instance, an RPL spectrum with $\gamma = 2.5$ and $\beta = -0.1$ could explain the NANOGrav signal and would be consistent with the CMB bound. However, all positively curved parabolas are in conflict with the $\Delta N_{\rm eff}$ and LVK bounds—as long as we assume that the RPL spectrum does indeed extend all the way up to LVK frequencies and beyond.

For a sufficiently low reheating temperature and hence sufficiently low cutoff frequency in the GWB spectrum, the $\Delta N_{\rm eff}$ and LVK bounds can always be avoided (see our analysis in A. Afzal et al. 2023, in which we also consider the

possibility of a very low reheating temperature). Furthermore, it goes without saying that the bounds in Figure 4 represent the specific CMB, LVK, and $\Delta N_{\rm eff}$ bounds on the specific model that we are interested in in this Letter, the RPL model, if we interpret this model as a simple description of IGWs. From our analysis, we are not able to draw any model-independent conclusions about the dynamics of inflation in general.

Finally, we emphasize that the $\Delta N_{\rm eff}$ and LVK bounds require β to be strictly positive. Even the case $\beta = 0$, i.e., the CPL model, is ruled out. This represents an important result of our analysis and a crucial distinction between the minimal CPL model and the next-to-minimal RPL model. If the GWB signal seen in the PTA band should be of inflationary origin, the CPL model would not provide a viable description of this signal that could be extrapolated to very low and high frequencies; the RPL model, on the other hand, does.

5. Conclusions

In this Letter, we introduced a new model-agnostic template for the spectrum of the GWB signal in the PTA band: the RPL model, which generalizes the simplest spectral template, i.e., the CPL model, by allowing for a logarithmic frequency dependence of the spectral index. In the first part of the Letter, we fitted the RPL model to the NG15 data, which provided us with point and interval estimates for the three RPL parameters A, γ, and β. We find that, at present, the NG15 data are consistent with the assumption of no running of the spectral index, $\beta = 0$, which is reflected in a broad 95% credible interval, $\beta \in [-0.80, 2.96]$, and an inconclusive Bayes factor, $\mathcal{B} = 0.69 \pm 0.01$. At the same time, $\beta = 0$ is not contained in its 68% credible interval, $\beta \in [0.01, 1.90]$, which nourishes the hope that future PTA data sets may have a chance to find evidence for nonzero β and hence deviations from a pure CPL signal. Such a measurement would be instrumental for model selection. In particular, we propose to use the predicted value of β in astrophysical and cosmological GWB models as an additional discriminator among different theoretical models.

In the second part of the Letter, we subsequently interpreted the RPL model as a description of an IGW signal, which allowed us to combine the results of our Bayesian fit analysis with upper limits on IGWs at low and high frequencies. Remarkably enough, we found that parabola-shaped GWB spectra of inflationary origin with $\beta > 0$ (i.e., negatively curved spectra) can explain the NANOGrav signal while at the same time remaining consistent with bounds from BBN, the CMB, and LVK. This is a major success of the RPL model, distinguishing it from the CPL model, for which the same conclusion cannot be drawn. Our results thus motivate theoretical efforts toward the construction of explicit microscopic models of inflation that can achieve the required A, γ, and β values identified in this work.

Acknowledgments

L.B. acknowledges support from the National Science Foundation under award AST-1909933 and from the Research Corporation for Science Advancement under Cottrell Scholar Award No. 27553. P.R.B. is supported by the Science and Technology Facilities Council, grant No. ST/W000946/1. S. B. gratefully acknowledges the support of a Sloan Fellowship and the support of NSF under award #1815664. M.C. and S.R. T. acknowledge support from NSF AST-2007993. M.C. was supported by the Vanderbilt Initiative in Data Intensive Astrophysics (VIDA) Fellowship. Support for this work was provided by the NSF through the Grote Reber Fellowship Program administered by Associated Universities, Inc./National Radio Astronomy Observatory. Pulsar research at UBC is supported by an NSERC Discovery Grant and by CIFAR. K.C. is supported by a UBC Four Year Fellowship (6456). M.E.D. acknowledges support from the Naval Research Laboratory by NASA under contract S-15633Y. T. D. and M.T.L. are supported by an NSF Astronomy and Astrophysics Grant (AAG) award number 2009468. E.C.F. is supported by NASA under award number 80GSFC21M0002. G.E.F., S.C.S., and S.J.V. are supported by NSF award PHY-2011772. K.A.G. and S.R.T. acknowledge support from an NSF CAREER award #2146016. A.D.J. and M.V. acknowledge support from the Caltech and Jet Propulsion Laboratory President's and Director's Research and Development Fund. A. D.J. acknowledges support from the Sloan Foundation. The work of N.La., X.S., and D.W. is partly supported by the George and Hannah Bolinger Memorial Fund in the College of Science at Oregon State University. N.La. acknowledges the support from the Larry W. Martin and Joyce B. O'Neill Endowed Fellowship in the College of Science at Oregon State University. Part of this research was carried out at the Jet Propulsion Laboratory, California Institute of Technology, under a contract with the National Aeronautics and Space Administration (80NM0018D0004). R.R.L.d.S. is supported in part by the National Science Centre (Poland) under the research grant No. 2020/38/E/ST2/00126. D.R.L. and M.A.M. are supported by NSF #1458952. M.A.M. is supported by NSF #2009425. C.M.F.M. was supported in part by the National Science Foundation under grant Nos. NSF PHY-1748958 and AST-2106552. A.Mi. is supported by the Deutsche Forschungsgemeinschaft under Germany's Excellence Strategy–EXC 2121 Quantum Universe–390833306. The Dunlap Institute is funded by an endowment established by the David Dunlap family and the University of Toronto. K.D.O. was supported in part by NSF grant No. 2207267. T.T.P. acknowledges support from the Extragalactic Astrophysics Research Group at Eötvös Loránd University, funded by the Eötvös Loránd Research Network (ELKH), which was used during the development of this research. H.A.R. is supported by NSF Partnerships for Research and Education in Physics (PREP) award No. 2216793. S.M.R. and I.H.S. are CIFAR Fellows. Portions of this work performed at NRL were supported by ONR 6.1 basic research funding. J.D.R. also acknowledges support from start-up funds from Texas Tech University. The work of K.Sc., T.S., and R.v.E. is supported by Deutsche Forschungsgemeinschaft (DFG) through the Research Training Group (Graduiertenkolleg) 2149: Strong and Weak Interactions–from Hadrons to Dark Matter. J.S. is supported by an NSF Astronomy and Astrophysics Postdoctoral Fellowship under award AST-2202388 and acknowledges previous support by the NSF under award 1847938. C.U. acknowledges support from BGU (Kreitman fellowship) and the Council for Higher Education and Israel Academy of Sciences and Humanities (Excellence fellowship). C.A.W. acknowledges support from CIERA, the Adler Planetarium, and the Brinson Foundation through a CIERA-Adler postdoctoral fellowship. O.Y. is supported by the National Science Foundation Graduate Research Fellowship under grant No. DGE-2139292.

Author Contributions

This Letter uses over a decade's worth of pulsar timing observations and is the product of the work of many people. K. Sc. initiated and led the project, designed the analysis, carried out the analytical calculations, and wrote the manuscript. R.R. L.d.S. carried out the MCMC analysis and prepared all figures. D.E. cross-checked parts of the MCMC analysis. R.v.E. and T. Sc. cross-checked and evaluated the parameter bounds in Section 4. The authors thank Andrew Casey-Clyde for suggesting additional references, Timothy Dolch and Ken Olum for helpful feedback and comments on the manuscript, and all members of the NANOGrav New Physics Working Group who provided feedback and comments in working group meetings.

Data Set

G.A., A.A., A.M.A., Z.A., P.T.B., P.R.B., H.T.C., K.C., M. E.D., P.B.D., T.D., E.C.F., W.F., E.F., G.E.F., N.G.D., D.C.G., P.A.G., J.G., R.J.J., M.L.J., D.L.K., M.K., M.T.L., D.R.L., J. L., R.S.L., A.M., M.A.M., N.M., B.W.M., C.N., D.J.N., T.T. N., B.B.P.P., N.S.P., H.A.R., S.M.R., P.S.R., A.S., C.S., B.J.S. A., I.H.S., K.St., A.S., J.K.S., and H.M.W. developed timing models and ran observations for the NG15 data set.

Computing Resources

Part of this work was conducted using the High Performance Computing Cluster PALMA II at the University of Münster.[73] The use of the CIS computer cluster at the National Centre for Nuclear Research in Warsaw is gratefully acknowledged.

Funding Information

The NANOGrav Collaboration receives support from National Science Foundation (NSF) Physics Frontiers Center award Nos. 1430284 and 2020265, the Gordon and Betty Moore Foundation, NSF AccelNet award No. 2114721, an NSERC Discovery Grant, and CIFAR. The Arecibo Observatory is a facility of the NSF operated under cooperative agreement (AST-1744119) by the University of Central Florida (UCF) in alliance with Universidad Ana G. Méndez (UAGM) and Yang Enterprises (YEI), Inc. The Green Bank Observatory is a facility of the NSF operated under cooperative agreement by Associated Universities, Inc. The National Radio Astronomy Observatory is a facility of the NSF operated under cooperative agreement by Associated Universities, Inc.

ORCID iDs

Gabriella Agazie https://orcid.org/0000-0001-5134-3925
Akash Anumarlapudi https://orcid.org/0000-0002-8935-9882
Anne M. Archibald https://orcid.org/0000-0003-0638-3340
Jeremy G. Baier https://orcid.org/0000-0002-4972-1525
Paul T. Baker https://orcid.org/0000-0003-2745-753X
Bence Bécsy https://orcid.org/0000-0003-0909-5563
Laura Blecha https://orcid.org/0000-0002-2183-1087
Adam Brazier https://orcid.org/0000-0001-6341-7178
Paul R. Brook https://orcid.org/0000-0003-3053-6538
Sarah Burke-Spolaor https://orcid.org/0000-0003-4052-7838
J. Andrew Casey-Clyde https://orcid.org/0000-0002-5557-4007
Maria Charisi https://orcid.org/0000-0003-3579-2522
Shami Chatterjee https://orcid.org/0000-0002-2878-1502
Tyler Cohen https://orcid.org/0000-0001-7587-5483
James M. Cordes https://orcid.org/0000-0002-4049-1882
Neil J. Cornish https://orcid.org/0000-0002-7435-0869
Fronefield Crawford https://orcid.org/0000-0002-2578-0360
H. Thankful Cromartie https://orcid.org/0000-0002-6039-692X
Kathryn Crowter https://orcid.org/0000-0002-1529-5169
Megan E. DeCesar https://orcid.org/0000-0002-2185-1790
Paul B. Demorest https://orcid.org/0000-0002-6664-965X
Lankeswar Dey https://orcid.org/0000-0002-2554-0674
Timothy Dolch https://orcid.org/0000-0001-8885-6388
Elizabeth C. Ferrara https://orcid.org/0000-0001-7828-7708
William Fiore https://orcid.org/0000-0001-5645-5336
Emmanuel Fonseca https://orcid.org/0000-0001-8384-5049
Gabriel E. Freedman https://orcid.org/0000-0001-7624-4616
Emiko C. Gardiner https://orcid.org/0000-0002-8857-613X
Nate Garver-Daniels https://orcid.org/0000-0001-6166-9646
Peter A. Gentile https://orcid.org/0000-0001-8158-683X
Joseph Glaser https://orcid.org/0000-0003-4090-9780
Deborah C. Good https://orcid.org/0000-0003-1884-348X
Kayhan Gültekin https://orcid.org/0000-0002-1146-0198
Jeffrey S. Hazboun https://orcid.org/0000-0003-2742-3321
Ross J. Jennings https://orcid.org/0000-0003-1082-2342
Aaron D. Johnson https://orcid.org/0000-0002-7445-8423
Megan L. Jones https://orcid.org/0000-0001-6607-3710
David L. Kaplan https://orcid.org/0000-0001-6295-2881
Luke Zoltan Kelley https://orcid.org/0000-0002-6625-6450
Matthew Kerr https://orcid.org/0000-0002-0893-4073
Joey S. Key https://orcid.org/0000-0003-0123-7600
Nima Laal https://orcid.org/0000-0002-9197-7604
Michael T. Lam https://orcid.org/0000-0003-0721-651X
William G. Lamb https://orcid.org/0000-0003-1096-4156
Natalia Lewandowska https://orcid.org/0000-0003-0771-6581
Rafael R. Lino dos Santos https://orcid.org/0000-0002-7996-5045
Tingting Liu https://orcid.org/0000-0001-5766-4287
Duncan R. Lorimer https://orcid.org/0000-0003-1301-966X
Jing Luo https://orcid.org/0000-0001-5373-5914
Ryan S. Lynch https://orcid.org/0000-0001-5229-7430
Chung-Pei Ma https://orcid.org/0000-0002-4430-102X
Dustin R. Madison https://orcid.org/0000-0003-2285-0404
Alexander McEwen https://orcid.org/0000-0001-5481-7559
James W. McKee https://orcid.org/0000-0002-2885-8485
Maura A. McLaughlin https://orcid.org/0000-0001-7697-7422
Natasha McMann https://orcid.org/0000-0002-4642-1260
Bradley W. Meyers https://orcid.org/0000-0001-8845-1225
Patrick M. Meyers https://orcid.org/0000-0002-2689-0190
Chiara M. F. Mingarelli https://orcid.org/0000-0002-4307-1322
Andrea Mitridate https://orcid.org/0000-0003-2898-5844
Cherry Ng https://orcid.org/0000-0002-3616-5160
David J. Nice https://orcid.org/0000-0002-6709-2566
Stella Koch Ocker https://orcid.org/0000-0002-4941-5333

[73] https://www.uni-muenster.de/IT/HPC

Ken D. Olum https://orcid.org/0000-0002-2027-3714
Timothy T. Pennucci https://orcid.org/0000-0001-5465-2889
Benetge B. P. Perera https://orcid.org/0000-0002-8509-5947
Nihan S. Pol https://orcid.org/0000-0002-8826-1285
Henri A. Radovan https://orcid.org/0000-0002-2074-4360
Scott M. Ransom https://orcid.org/0000-0001-5799-9714
Paul S. Ray https://orcid.org/0000-0002-5297-5278
Joseph D. Romano https://orcid.org/0000-0003-4915-3246
Jessie C. Runnoe https://orcid.org/0000-0001-8557-2822
Alexander Saffer https://orcid.org/0000-0001-7832-9066
Shashwat C. Sardesai https://orcid.org/0009-0006-5476-3603
Ann Schmiedekamp https://orcid.org/0000-0003-4391-936X
Carl Schmiedekamp https://orcid.org/0000-0002-1283-2184
Kai Schmitz https://orcid.org/0000-0003-2807-6472
Tobias Schröder https://orcid.org/0000-0002-4658-2857
Brent J. Shapiro-Albert https://orcid.org/0000-0002-7283-1124
Xavier Siemens https://orcid.org/0000-0002-7778-2990
Joseph Simon https://orcid.org/0000-0003-1407-6607
Magdalena S. Siwek https://orcid.org/0000-0002-1530-9778
Sophia V. Sosa Fiscella https://orcid.org/0000-0002-5176-2924
Ingrid H. Stairs https://orcid.org/0000-0001-9784-8670
Daniel R. Stinebring https://orcid.org/0000-0002-1797-3277
Kevin Stovall https://orcid.org/0000-0002-7261-594X
Abhimanyu Susobhanan https://orcid.org/0000-0002-2820-0931
Joseph K. Swiggum https://orcid.org/0000-0002-1075-3837
Stephen R. Taylor https://orcid.org/0000-0003-0264-1453
Jacob E. Turner https://orcid.org/0000-0002-2451-7288
Caner Unal https://orcid.org/0000-0001-8800-0192
Michele Vallisneri https://orcid.org/0000-0002-4162-0033
Rutger van Haasteren https://orcid.org/0000-0002-6428-2620
Sarah J. Vigeland https://orcid.org/0000-0003-4700-9072
Richard von Eckardstein https://orcid.org/0009-0006-9176-2343
Haley M. Wahl https://orcid.org/0000-0001-9678-0299
Caitlin A. Witt https://orcid.org/0000-0002-6020-9274
David Wright https://orcid.org/0000-0003-1562-4679
Olivia Young https://orcid.org/0000-0002-0883-0688

References

Abbott, L. F., & Wise, M. B. 1984, NuPhB, 244, 541
Abbott, R., Abbott, T.D., Abraham, S., et al. 2021, PhRvD, 104, 022004
Afzal, A., Agazie, G., Anumarlapudi, A., et al. 2023, ApJL, 951, L11
Agazie, G., Anumarlapudi, A., Archibald, A.M., et al. 2023a, ApJL, 951, L8
Agazie, G., Alam, M.F., Anumarlapudi, A., et al. 2023b, ApJL, 951, L9
Agazie, G., Anumarlapudi, A., Archibald, A.M., et al. 2023c, ApJL, 952, L37
Agazie, G., Anumarlapudi, A., Archibald, A.M., et al. 2023d, ApJL, 951, L50
Agazie, G., Anumarlapudi, A., Archibald, A.M., et al. 2023e, ApJL, 956, L3
Agazie, G., Anumarlapudi, A., Archibald, A.M., et al. 2023f, ApJL, 951, L10
Agazie, G., Anumarlapudi, A., Archibald, A.M., et al. 2025, ApJ, 978, 31
Aghanim, N., Akrami, Y., Ashdown, M., et al. 2020, A&A, 641, A6
Akrami, Y., Arroja, F., Ashdown, M., et al. 2020, A&A, 641, A10
Antoniadis, J., Arumugam, P., Arumugam, S., et al. 2023, A&A, 678, A50
Antoniadis, J., Arumugam, P., Arumugam, S., et al. 2024, A&A, 685, A94
Arzoumanian, Z., Brazier, A., Burke-Spolaor, S., et al. 2015, ApJ, 813, 65
Ben-Dayan, I., Kumar, U., Thattarampilly, U., & Verma, A. 2023, PhRvD, 108, 103507
Benetti, M., Graef, L. L., & Vagnozzi, S. 2022, PhRvD, 105, 043520
Caprini, C., & Figueroa, D. G. 2018, CQGra, 35, 163001
Caprini, C., Jinno, R., Lewicki, M., et al. 2024, JCAP, 2024, 020
Carlin, B. P., & Chib, S. 1995, J. R. Stat. Soc. Ser. B Stat. Method, 57, 473
Drewes, M., Georis, Y., Klasen, M., Wiggering, L. P., & Wong, Y. Y. Y. 2024, JCAP, 06, 032
Efron, B., & Tibshirani, R. 1986, StaSc, 57, 54
Ellis, J., & van Haasteren, R. 2017, jellis18/PTMCMCSampler: Official Release, v1.0.0, Zenodo, doi:10.5281/zenodo.1037579
Ellis, J. A., Vallisneri, M., Taylor, S. R., & Baker, P. T., 2019 ENTERPRISE: Enhanced Numerical Toolbox Enabling a Robust PulsaR Inference SuitE, Astrophysics Source Code Library, ascl:1912.015
Fabbri, R., & Pollock, M. d. 1983, PhLB, 125, 445
Galloni, G., Henrot-Versillé, S., & Tristram, M. 2024, PhRvD, 110, 063511
Gersbach, K. A., Taylor, S. R., Meyers, P. M., & Romano, J. D. 2024, arXiv:2406.11954
Godsill, S. J. 2001, J. Comput. Graph. Stat., 10, 230
Grishchuk, L. P. 1974, ZhETF, 67, 825
Guzzetti, M. C., Bartolo, N., Liguori, M., & Matarrese, S. 2016, NCimR, 39, 399
Hee, S., Handley, W. J., Hobson, M. P., & Lasenby, A. N. 2015, MNRAS, 455, 2461
Hellings, R. W., & Downs, G. S. 1983, ApJL, 265, L39
Johnson, A.D., Meyers, P.M., Baker, P.T., et al. 2024, PhRvD, 109, 103012
Jones, M.L., McLaughlin, M.A., Lam, M.T., et al. 2017, ApJ, 841, 125
Kamionkowski, M., & Riess, A. G. 2023, ARNPS, 73, 153
Kinney, W. H. 2021, arXiv:2103.00281
Kocsis, B., & Sesana, A. 2011, MNRAS, 411, 1467
Kuroyanagi, S., Takahashi, T., & Yokoyama, S. 2021, JCAP, 01, 071
Lamb, W. G., Taylor, S. R., & van Haasteren, R. 2023, PhRvD, 108, 103019
Lentati, L., Alexander, P., Hobson, M.P., et al. 2013, PhRvD, 87, 104021
Lewis, A. 2019, arXiv:1910.13970
Liddle, A. R., & Lyth, D. H. 2000, Cosmological Inflation and Large-Scale Structure (Cambridge: Cambridge Univ. Press)
Mitridate, A., Wright, D., von Eckardstein, R., et al. 2023, arXiv:2306.16377
Nakayama, K., Saito, S., Suwa, Y., & Yokoyama, J. 2008, JCAP, 06, 020
Phinney, E. S. 2001, arXiv:astro-ph/0108028
Pisanti, O., Mangano, G., Miele, G., & Mazzella, P. 2021, JCAP, 04, 020
Reardon, D.J., Zic, A., Shannon, R.M., et al. 2023, ApJL, 951, L6
Rubakov, V. A., Sazhin, M. V., & Veryaskin, A. V. 1982, PhLB, 115, 189
Saikawa, K., & Shirai, S. 2018, JCAP, 05, 035
Saikawa, K., & Shirai, S. 2020, JCAP, 08, 011
Sesana, A., Vecchio, A., & Colacino, C. N. 2008, MNRAS, 390, 192
Starobinsky, A. A. 1979, JETPL, 30, 682
Taylor, S. R. 2021, arXiv:2105.13270
Taylor, S. R., Baker, P. T., Hazboun, J. S., Simon, J., & Vigeland, S. J., 2021 enterprise_extensions, v2.4.3, Github, https://github.com/nanograv/enterprise_extensions
Tristram, M., Banday, A.J., Górski, K. M., et al. 2022, PhRvD, 105, 083524
Vagnozzi, S. 2021, MNRAS, 502, L11
Vagnozzi, S. 2023, JHEAp, 39, 81
van Haasteren, R., & Levin, Y. 2013, MNRAS, 428, 1147
Xu, H., Chen, S., Guo, Y., et al. 2023, RAA, 23, 075024
Yeh, T.-H., Olive, K. A., & Fields, B. D. 2021, JCAP, 03, 046